Official Journal of CIOMP
elight.springeropen.com

LETTER

Open Access

Lead halide perovskite sensitized WSe_2 photodiodes with ultrahigh open circuit voltages

Sung-Joon Lee[1,2,4†], Hung-Chieh Cheng[1†], Yiliu Wang[3], Boxuan Zhou[1], Dehui Li[3], Gongming Wang[3], Yuan Liu[1], Jian Guo[1], Hao Wu[1], Dae Joon Kang[2*], Yu Huang[1*] and Xiangfeng Duan[3*]

Abstract

Two-dimensional semiconductors (2DSCs) have attracted considerable interests for optoelectronic devices, but are often plagued by the difficulties in tailoring the charge doping type and poor optical absorption due to their atomically thin geometry. Herein, we report a methylammonium lead iodide perovskite ($CH_3NH_3PbI_3$)/2DSC heterojunction device, in which the electric-field controllable ion migration in the perovskite layer is exploited to induce reversible electron- and hole-doping effects in the underlying monolayer tungsten diselenide (WSe_2) to form a programmable p–n photodiode. At the same time, the $CH_3NH_3PbI_3$ layer functions as a highly efficient sensitization layer to greatly boost the optical absorption and external quantum efficiency (EQE) of the resulting photodiode. By asymmetrically poling the perovskite layer, gold-contacted $CH_3NH_3PbI_3/WSe_2$ devices show a switchable open circuit voltage up to 0.78 V, along with a high EQE of 84.3%. The integration of tunable graphene-contacts further improves the photodiode performance to achieve a highest open circuit voltage of 1.08 V and a maximum EQE of 91.3%, greatly exceeding those achieved previously in 2DSC lateral diodes. Our studies establish a non-invasive approach to switch optoelectronic functions and open up a new avenue toward high-performance reconfigurable optoelectronic devices from 2DSCs.

Keywords Electrostatic doping, Programmable optoelectronic devices, Lead halide perovskite, Two-dimensional materials, Ion migration, Photodiodes

1 Introduction

Electrostatic doping has been widely used in low-dimensional materials, including carbon nanotube (CNT), and two-dimensional (2D) materials such as graphene and transition metal dichalcogenides (TMDs) [1–10]. Unlike conventional lattice doping with impurity atoms [11], it is difficult to achieve doping in nanoscale materials due to the limited physical space. The electrostatic doping opens an effective pathway to tune the charge carriers in nanoscale materials without introducing impurity atoms which can perturb the atomic arrangement and degrade the intrinsic electronic properties of the nanoscale materials [12]. Recently, ionic solids have been explored for creating a p–n junction in monolayer 2D materials in which the frozen mobile ions provide electrostatic fields

†Sung-Joon Lee and Hung-Chieh Cheng contributed equally to this work

*Correspondence:
Dae Joon Kang
djkang@skku.edu
Yu Huang
yhuang@seas.ucla.edu
Xiangfeng Duan
xduan@chem.ucla.edu
[1] Department of Materials Science and Engineering, University of California, Los Angeles, CA, USA
[2] Department of Physics, Sungkyunkwan University, Suwon, Republic of Korea
[3] Department of Chemistry and Biochemistry, University of California, Los Angeles, CA, USA
[4] Present Address: Materials Science and Technology Division, U.S. Naval Research Laboratory, Washington, DC, USA

to modulate the carrier density of underlying 2D semiconducting channel. Due to the well-defined shape of ionic solid, local control of the doping on 2D semiconductors (2DSCs) allows diverse designs for integration of solid-state electronic/optoelectronic devices with minimum crosstalk. For example, the manipulation of silver ions in solid-state superionic silver iodide (AgI) was employed for tailoring the carrier type of 2DSCs to achieve reversibly programmable transistors, diodes, photodiodes and logic gates [13].

To date, the monolayer TMDs have been widely adopted in novel optoelectronic applications such as electrically tunable light-emitting diodes (LEDs) [14], gate-controlled p–n junction diodes [15], and solar cells [16]. However, the monolayer TMDs also exhibit some intrinsic limits for high-performance optoelectronic applications. In particular, incorporation of impurity dopants in the atomically thin 2D lattices has been fundamentally limited by the little physical space in the atomically thin lattices. It has been a persistent challenge to controllably tailor the charge doping type/density in monolayer 2DSCs using selected lattice dopants. Consequently, the p–n photodiodes made from 2DSCs to date are often plagued by non-ideal contacts at either p- or n-side, which limits the achievable open circuit voltage (V_{OC}). Additionally, total light absorption and spectral sensitivity of 2DSCs are fundamentally limited by their atomically thin geometry [17], compromising the photocarrier generation efficiency and the achievable external quantum efficiency (EQE). Considerable efforts have been devoted to overcoming such intrinsic limitations by heterogeneously integrating with other well-known optoelectronic materials [18–20]. For example, interfacing with organic dye molecules has been demonstrated as an effective strategy to control its optoelectrical properties [21].

The hybrid lead halide perovskites (LHPs) have received substantial attention for photovoltaics due to their excellent optoelectronic performance and low fabrication cost [22]. Despite its extraordinary potential, the "soft lattice" ionic LHPs are typically plagued with ion migrations under voltage bias, leading to poor material stability [23, 24] and large hysteresis in the voltage-dependent photocurrents [25, 26]. The migration of positively or negatively charged ions could induce ion accumulation or ionic charge imbalance under applied electric fields [27]. Here, we exploit such ionic charge imbalance in LHPs to induce reversible doping in nearby 2DSCs to create high-performance photodiodes.

Methylammonium lead iodide ($CH_3NH_3PbI_3$ or $MAPbI_3$) represents the most prominent examples of LHPs with excellent optical absorption and photoresponsive properties [28], but is seriously plagued by ionic motion [29]. Although undesirable for stable operation of solar cell applications [30], the accumulation of ionic charge from the bias-induced ions migration in $MAPbI_3$ can be exploited for selectively doping nearby 2DSCs to create perovskite-sensitized 2D photodiodes with high optoelectronic performance. In this regard, the atomically thin 2DSCs are ideally suited for efficiently coupling with the ionic solids that serve as a non-covalent doping agent to reversibly induce reconfigurable p-type or n-type doping effect. Such tunable doping effect further offers a new class of 2DSC-based photodiodes with switchable polarities. With van der Waals integration [31] of ionic solids with excellent optoelectronic properties, the 2D diodes formed from ionic-doping effect provide an efficient way to extract photogenerated carriers in $MAPbI_3$.

2 Results and discussion

2.1 Doping effect of $MAPbI_3$ perovskite on WSe_2 field-effect transistor

To elucidate the electrostatic doping effect introduced by $MAPbI_3$ perovskite, the Au-contacted two-terminal monolayer WSe_2 field-effect transistors (FETs) (Additional file 1: Fig. S1) on top of highly doped (p^{++}) silicon covered with 290-nm SiO_2 were adopted for their ambipolarity [32]. The ambipolar nature of WSe_2 is amenable for achieving both n-type and p-type doping effects, which is essential for forming photodiode and efficiently extracting the photogenerated electrons and holes (Fig. 1). The $MAPbI_3$ perovskite was integrated on top of the WSe_2 device through an aligned transfer of lead iodide (PbI_2) flake [33, 34] followed by vapor phase thermal conversion process under methylammonium iodide (CH_3NH_3I) vapor [35–37], producing an overall device structure of: $MAPbI_3$/Au-WSe_2-Au on a SiO_2/Si substrate (Fig. 1a and Additional file 1: Fig. S2). Our previous studies [36, 37] showed that, after the conversion process, a prominent single photoluminescence peak of $MAPbI_3$ perovskite was located at around ~1.63 eV, indicating a successful conversion from PbI_2 to $MAPbI_3$ perovskite. All the $MAPbI_3$/WSe_2 FETs were encapsulated within few-layer hexagonal boron nitride (h-BN) to prevent surface degradation of $MAPbI_3$ perovskite under ambient conditions [23, 38].

As a reference, WSe_2 FET was studied before van der Waals integration with $MAPbI_3$ perovskite (Fig. 2a). Transfer characteristics (I_{DS}-V_{BG}) of the WSe_2 FET showed ambipolar behavior with a slight p-doping effect. After $MAPbI_3$ integration, the $MAPbI_3$/WSe_2 FET showed a strong p-type doping effect with the drain-source current (I_{DS}) (Fig. 2b) increased by about 2–5 orders of magnitude compared to that of WSe_2 FET. The resulting p-type doping effect of the WSe_2

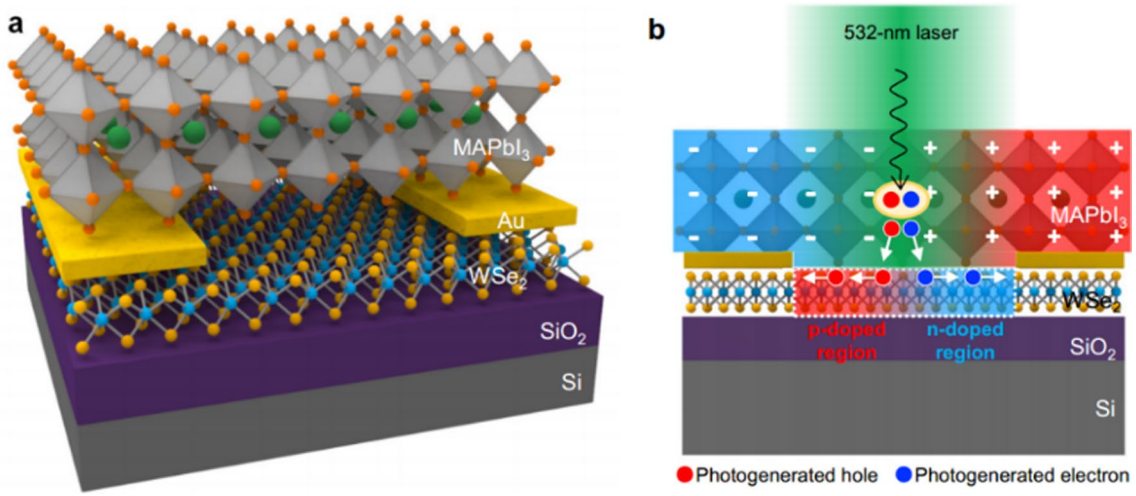

Fig. 1 Illustrations of WSe_2 FET integrated with $MAPbI_3$ perovskite to form a programmable perovskite sensitized photodiode. **a** Schematic illustration of the $MAPbI_3/WSe_2$ FET device structure. **b** Schematic illustration of the extraction of photogenerated carriers from $MAPbI_3$ into polarized WSe_2 diode channel

channel can be attributed to the charge transfer in the $MAPbI_3/WSe_2$ heterojunction [39]. On the other hand, the drain-source current of the $MAPbI_3$ FET without monolayer WSe_2 was essentially at the baseline of the measurement resolution (Fig. 2c), about 4–5 orders of magnitude smaller than that of the $MAPbI_3/WSe_2$ FET. This result indicates that the $MAPbI_3$ perovskite itself does not directly contribute to significant charge transport in the $MAPbI_3/WSe_2$ device but primarily serves as a doping agent to greatly increase carrier density in monolayer WSe_2.

By comparing the device current measured under light illumination and dark conditions in transfer curves (I_{DS}-V_{BG} at $V_{DS}=5$ V), we have determined the photocurrents ($I_{ph}=I_{light}-I_{dark}$) for WSe_2 FET ($I_{ph,WSe2}$), $MAPbI_3$ FET ($I_{ph,perov}$) and $MAPbI_3/WSe_2$ FET ($I_{ph,hetero}$) (Fig. 2d). The photocurrent observed in WSe_2 FET ($I_{ph,WSe2}$) is rather low due to low optical absorption in the atomically thin WSe_2. Similarly, the photocurrent observed in $MAPbI_3$ FET ($I_{ph,perov}$) is also rather low, which might be largely attributed to the poor charge transport properties in $MAPbI_3$. In contrast, the I_{ph} achieved in $MAPbI_3/WSe_2$ FET ($I_{ph,hetero}$) is more than 4 orders of magnitude larger than the sum of the photocurrent achieved in WSe_2 FET ($I_{ph,WSe2}$) and $MAPbI_3$ FET ($I_{ph,perov}$), suggesting significant synergistic effects of $MAPbI_3/WSe_2$ heterostructure in efficient extracting the photocarriers. Such a synergistic effect can be attributed to efficient photon absorption and photocarrier generation in $MAPbI_3$ with excellent optical absorption properties, and the rapid separation and efficient transport of photocarriers by the WSe_2 channel with excellent charge transport properties [40].

2.2 Gate-controlled ionic doping effect

The above studies clearly demonstrate the doping effect by $MAPbI_3$ ionic solid can considerably tailor the charge transport properties of monolayer WSe_2 semiconductor. $MAPbI_3$ perovskite is also well known for its low activation energy for ion migration and bias-induced ion migration [41]. It is thus possible to create an ionic profile within $MAPbI_3$ ionic solid by applying external voltages to drive the ion movement to produce a charge imbalance between positively or negatively charged ions in the desired locations of $MAPbI_3$ perovskite (e.g., at the interface between perovskite and 2D material). These imbalanced ions near the $MAPbI_3/WSe_2$ interface can induce an electrostatic doping effect to the underlying WSe_2. To this end, we studied the feasibility of switching the majority carrier type in WSe_2 devices by applying vertical bias voltages to back-gate electrode in $MAPbI_3/WSe_2$ FET (Fig. 3a). WSe_2 devices fabricated on SiO_2/Si substrate typically show dominant p-type behavior that is difficult to reverse to n-type. In this regard, the $MAPbI_3/WSe_2$ FET was fabricated on a (3-aminopropyl) triethoxysilane (APTES) treated SiO_2/Si substrate, which provides n-doping effect to the WSe_2 channel [42]. By adopting the APTES-treated SiO_2/Si substrate, the p-doping effect in WSe_2 channel originated from the SiO_2/Si substrate can be suppressed. This facilitates a type-switchable doping effect to WSe_2 channel by mobile ions in $MAPbI_3$ perovskite ionic solid.

Previous studies indicate the I^- show considerable mobility under external bias [43], which allows an external voltage to drive the ion movement and induce the desired ionic doping effect. To examine

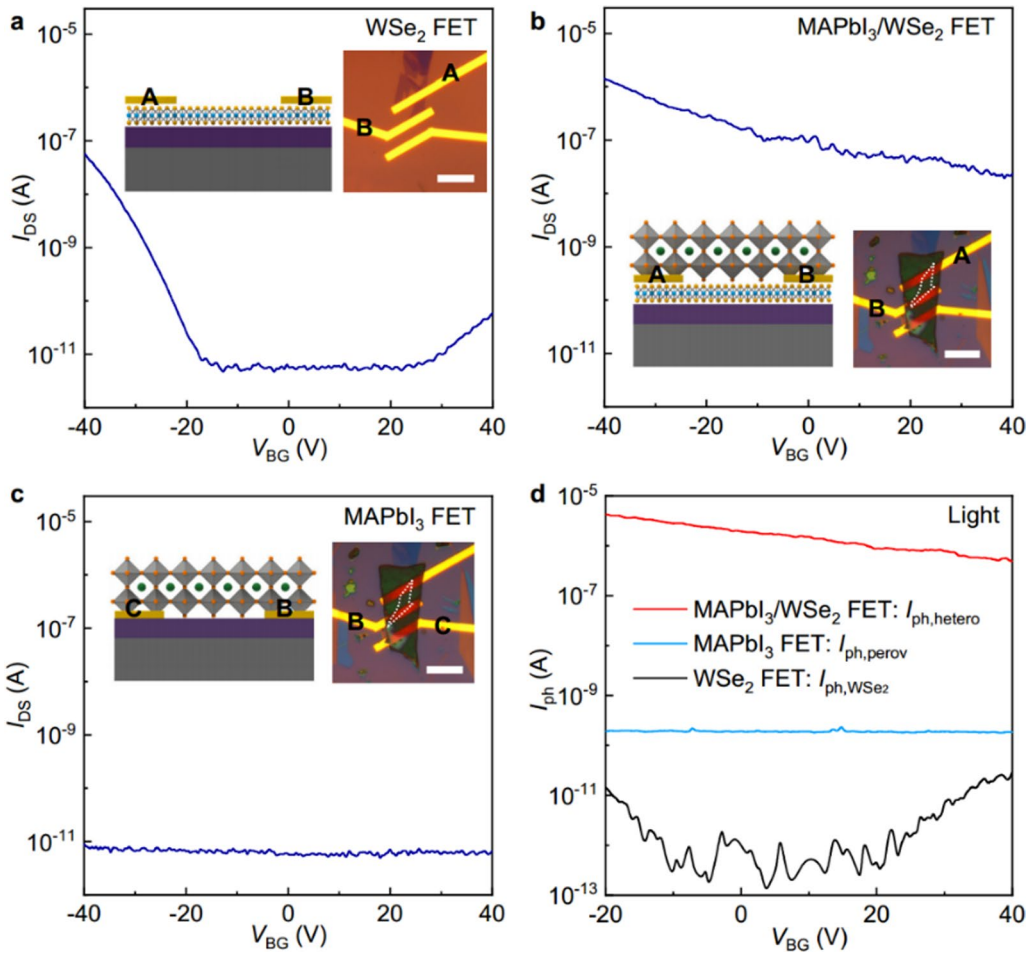

Fig. 2 Doping effects in $MAPbI_3/WSe_2$ heterostructure. **a**–**c** Transfer curves (I_{DS}-V_{BG}) of WSe_2 FET, $MAPbI_3/WSe_2$ FET and $MAPbI_3$ FET measured with A-B, A-B and C-B electrodes where A and C were used as drain electrodes and B was grounded. The insets (left) show schematic illustrations of each device structure. The insets (right) show the optical images of the devices, where the white dashed frames mark the position of WSe_2. The white scale bar is 10 μm. Each device was measured at $V_{DS} = 5$ V under dark condition. **d** Photocurrents (I_{ph}) of WSe_2 FET, $MAPbI_3$ FET and $MAPbI_3/WSe_2$ FET. Each device was measured at $V_{DS} = 5$ V under white light illumination condition

the doping effect induced by the accumulated mobile ions at the $MAPbI_3/WSe_2$ interface, a vertical electric field from back-gate electrode was applied against initial non-poled state. All the poling processes in this paper were conducted at 400 K to promote ion migration in $MAPbI_3$ perovskite. After 5 min of the electrical poling process, the device was cooled down to 79 K under the continuous poling voltage to freeze the ions at the designed location [44, 45]. For example, a negative back-gate electric field ($V_{BG} = -60$ V) pushes the negative ions (I^-) away from the $WSe_2/MAPbI_3$ interface, resulting in a net positive charge at the interface. This net positive charge can electrostatically increase electron concentration in WSe_2 channel, resulting in n-type FET. On the other hand, a positive poling gate bias attracts the I^- moving towards the $MAPbI_3/WSe_2$ interface, which increases the hole concentration in WSe_2 channel and produces a p-type FET.

The transfer curve (I_{DS}-V_{DS}) of the as-fabricated $MAPbI_3/WSe_2$ FET (Fig. 3a) showed p-type characteristics under dark condition at 79 K (Fig. 3d). After the negative vertical poling process (Fig. 3b), the transfer curve was shifted from p-type to n-type behavior, confirming that electrons became the dominant carrier type (Fig. 3e). It is important to note that the $MAPbI_3$ perovskite does not directly contribute to the charge transport of the FET (Fig. 2c) but only provides the electrostatic doping effect to modulate the dominant carrier type and concentration. To highlight the controllability of the doping effect, a positive back-gate bias voltage ($V_{BG} = 60$ V) was applied to the identical device against the previously n-programmed state during the poling process (Fig. 3c).

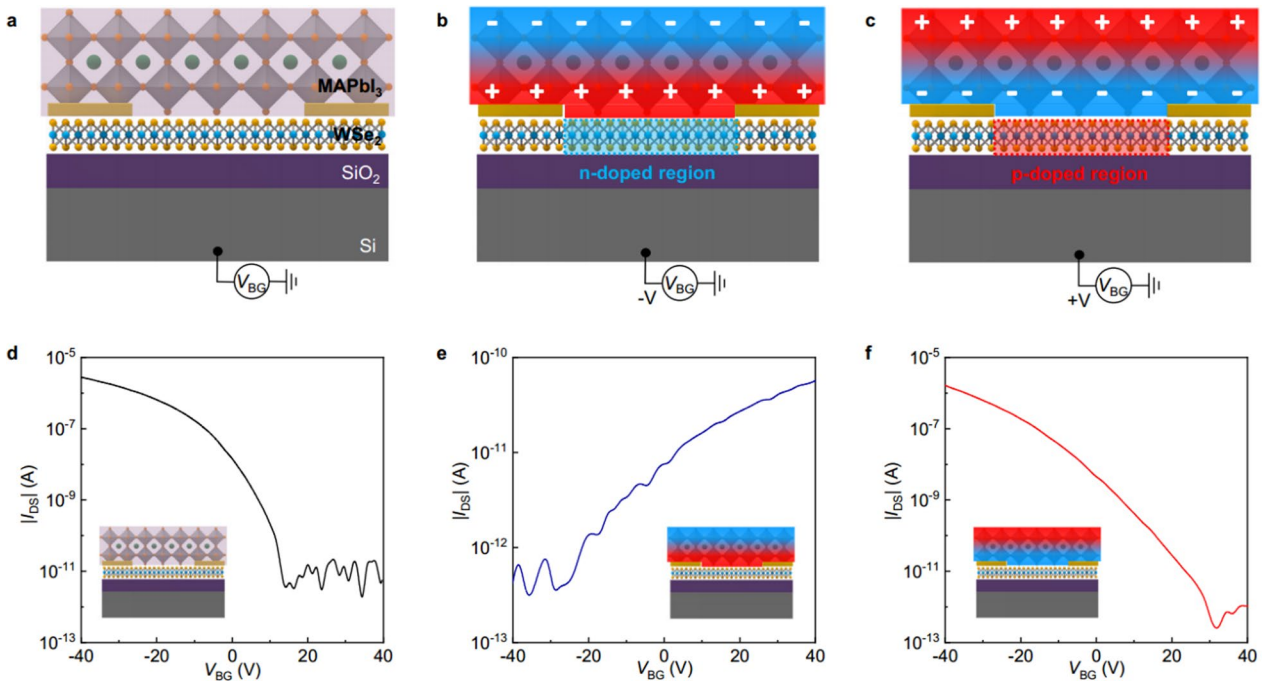

Fig. 3 Carrier type-switchable $MAPbI_3/WSe_2$ FETs. **a** Schematic illustration of as-fabricated $MAPbI_3/WSe_2$ FET. **b**, **c** Schematic illustrations of negative and positive back-gate poling process that enriches a net positive or negative ionic charge at $MAPbI_3/WSe_2$ interface. **d** Transfer curves (I_{DS}-V_{BG}) of as-fabricated $MAPbI_3/WSe_2$ FET. **e**, **f** Transfer curves (I_{DS}-V_{BG}) of $MAPbI_3/WSe_2$ FET after negative and positive back-gate poling processes, showing n- and p-channel FET characteristics. The insets show schematic illustrations of resulting ionic charge distribution. Each device was measured at $V_{DS} = 5$ V under dark condition

The results indicated the dominant carrier type was completely switched back to holes (Fig. 3f). The results suggested the vertical ionic poling process can be used to rationally tailor the dominant charge carrier type in $MAPbI_3/WSe_2$ heterostructure devices.

2.3 Drain-source-controlled ionic doping effect

The above studies clearly demonstrate reversible $MAPbI_3$ poling and WSe_2 doping with either electrons or holes. Taking a step further from the uniform poling with the vertical electric field, we have also exploited lateral electric fields for non-uniformly poling the ionic solid for asymmetric doping, and creation of a functional diode (Fig. 4a). In this case, ions in $MAPbI_3$ perovskite are polarized by the drain-source bias. The migration of ions in $MAPbI_3$ perovskite is driven by lateral electric field (V_{DS}), which leads to an ionic charge imbalance along the channel length. The resulting ionic profile induces opposite doping effects at both ends of the underlying WSe_2 channel. In the case of a negative bias lateral poling process, negative ions are accumulated near the grounded electrode (Fig. 4b). After the process, a net negative electrostatic potential is built up in the WSe_2 channel near grounded electrode, inducing p-type doping effect. On the other side of the WSe_2 channel near the biasing electrode, a net positive electrostatic potential is developed, inducing an n-type doping effect. Collectively, a forward biased n-p diode is created. In the same manner, a positive lateral poling process produces a forward biased p–n diode (Fig. 4c).

The output characteristics (I_{DS}-V_{DS}) of monolayer WSe_2 FET showed no current within $V_{DS} = \pm 1$ V at $V_{BG} = 0$ V under both dark and light illumination conditions (Additional file 1: Fig. S3). After lamination of $MAPbI_3$ perovskite and h-BN, the as-fabricated $MAPbI_3/WSe_2$ FET showed asymmetric output characteristics under dark condition (Fig. 4d). This initial output behavior might be attributed to Schottky barrier between WSe_2 channel and Au electrode at 79 K. After the negative poling process, rectifying output behavior exhibited a negative turn-on voltage and high output current beyond the turn-on voltage (Fig. 4e). To highlight the switchable doping effect, the lateral poling process with positive V_{DS} was conducted to the identical device. The rectification behavior of the diode was changed to the opposite polarity that showed a positive turn-on voltage and high output current in the positive bias regime (Fig. 4f). Such polarity-switchable rectification behavior demonstrates that the diode behavior is indeed resulted from

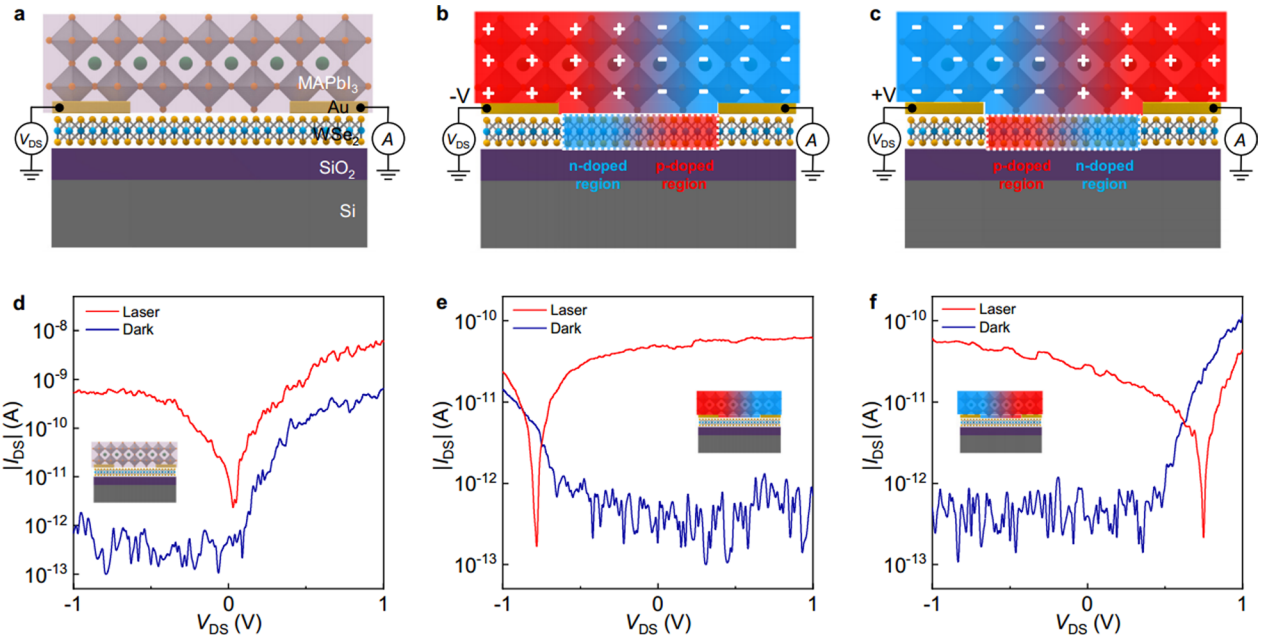

Fig. 4 Polarity-switchable $MAPbI_3/WSe_2$ diodes and photodiodes. **a** Schematic illustrations of as-fabricated $MAPbI_3/WSe_2$ device. **b**, **c** Schematic illustrations of non-uniform poling processes of resulting ionic charge distribution induced by negative and positive V_{DS}. The electrode on the left-hand side was used as a drain electrode and the other side was grounded. **d** Output curves (I_{DS}-V_{DS}) of the as-fabricated $MAPbI_3/WSe_2$ device. **e**, **f** Output curves (I_{DS}-V_{DS}) of the device after sequential lateral poling processes with negative and positive poling V_{DS}. The insets show schematic illustrations of resulting ionic charge profile. The measurements were conducted in dark (blue curve) and 532-nm laser illumination (Power density: 15 W/m^2, red curve)

poling-induced ionic doping effect rather than the non-ideal contact.

These programmed diodes can also function effective photodiodes. Under 532-nm laser excitation (15 W/m^2), the output characteristics of the as-fabricated $MAPbI_3/WSe_2$ FET showed a V_{OC} close to zero voltage, suggesting there was minimal extrinsic doping effect at this early state (Fig. 4d). The negatively poled photodiode delivered an V_{OC} of -0.78 V (Fig. 4e). After the positive lateral poling process, the identical photodiode showed a V_{OC} of $+0.75$ V very close to that of the negatively poled photodiode, demonstrating that the polarity is reversibly programmed by the poling process (Fig. 4f). The obtained V_{OC}s are comparable to the state-of-the-art results from previous reports (Additional file 1: Table S1).

To examine the optoelectronic performance of the $MAPbI_3/WSe_2$ photodiodes, a short-circuit photocurrent (I_{ph} at $V_{DS}=0$ V) of ~83.3 pA and a photoresponse time of ~450 μs was obtained (Additional file 1: Fig. S4). In addition, the external quantum efficiency (EQE) of the photodiode was extracted from the equation:

$$\mathrm{EQE} = \frac{I_{SC}}{P_{laser}A} \times \frac{hc}{e\lambda} \quad (1)$$

where the short-circuit current is I_{SC}, the power density of incident photons is P_{laser}, the effective area is A, the Planck's constant is h, the speed of light is c, the electron charge is e and the wavelength of the light is λ. The extracted EQE of 84.3% at 532 nm represents the highest value achieved from lateral or sensitized 2D diode at zero bias voltage ($V_{DS}=0$ V) (Additional file 1: Table S1) [46]. Such strong enhancement could be attributed to high optical absorption and long electron-carrier carrier diffusion length in $MAPbI_3$ perovskite [28, 47–50]. These excellent optoelectronic properties of the perovskite can ensure the photogenerated carriers in the $MAPbI_3$ to reach the p–n junction in the monolayer WSe_2 channel, where they are separated by the built-in potential and extracted to external circuit (Fig. 1b).

To elucidate the contribution of the measured photocurrent in the $MAPbI_3/WSe_2$ photodiode, we have examined the poling effect in both the $MAPbI_3$ FET (Fig. 2b) and the $MAPbI_3/WSe_2$ FET (Fig. 2c). The I_{DS}-V_{DS} curves were measured after the poling process for both devices (Additional file 1: Fig. S5). It is important to note that the $MAPbI_3/WSe_2$ device showed prominent rectification ratio under both dark ($>10^4$) and laser illumination ($>10^3$) conditions; while the $MAPbI_3$ device exhibited negligible currents or rectification ratio. Together, the rectification behavior and output currents were mainly contributed by the WSe_2 channel rather the $MAPbI_3$, and the $MAPbI_3$ mainly served as a tunable doping agent and

a sensitizer for significantly enhanced photon absorption efficiency and photocarrier generation.

2.4 Enhanced performance with graphene contact

Our findings show that the integration of the monolayer WSe_2 semiconductor and the $MAPbI_3$ ionic solid offers a type-switchable FET that can be reversibly programmed to either n-type or p-type characteristics depending on the direction of applied poling potentials. However, a single type of metal contact is not ideal for achieving optimized carrier transport at both n-type and p-type regions of the doped WSe_2 channel. Due to the fixed work-function of metal, one of the contacts could be non-ideal and form a Schottky barrier compromising the p–n diode effect. In this context, it is desirable to adopt a tunable work-function that can make optimal contacts either for electrons or holes. To this end, monolayer graphene was selected as tunable electrical contacts (Fig. 5a, b) for its electrostatically tunable work-functions [51–54]. Unlike metal electrodes, the work-function of graphene contact can be tuned by back-gate voltage or accumulated ions in the poled $MAPbI_3$ perovskite [13]. For the poled devices, the graphene contacts are electrostatically doped with electrons or holes by the poled $MAPbI_3$, with their work-function matching well with conduction or valence band edge of the WSe_2 channel electrostatically doped by the same poled $MAPbI_3$. The applied gate bias (V_{BG}) is used to further tune carrier type and concentration in WSe_2 to match with that of the doped graphene. In this case, a net positive charge in the $MAPbI_3$ perovskite increases the electron doping in graphene to reduce its work-function, and make it an optimum contact for n-type WSe_2 channel. Similarly, a net negative charge increases hole doping in graphene, increasing its work-function and making it a better contact for p-type WSe_2 channel.

Indeed, the graphene-contacted $MAPbI_3/WSe_2$ FET showed much larger gate-tunability (Fig. 5c) than the Au-contacted devices (Additional file 1: Fig. S6). This can be attributed to the effective modulation of the work-function of the graphene contact. In addition, the I_{DS}-V_{DS} curves under 532-nm laser illumination exhibited a wide gate-tunable V_{OC} from 0.03 to 1.08 V after positive poling process and a tunable V_{OC} from 0 to -0.96 V after negative poling process (Fig. 5d). The short circuit current measurement also shows a highly tunable EQE from 2.7 to 91.3% (Fig. 5e). It is important to note that, to be best of our knowledge, the V_{OC} of 1.08 V represents the highest V_{OC} ever achieved in WSe_2-based diodes in lateral structure, highlighting the excellent photodiode characteristics achieved in ion-doped p–n junctions (Additional file 1: Table S1). It should be noted that our study is fundamentally different from previous studies of photodetection using 2DSC/perovskite heterojunctions, in which the perovskite layer functions as a photogate and does not exhibit power generation [40, 49]. In contrast, the polarized perovskite in our study modifies the carrier type and creates a sensitized p–n photodiode in the 2DSC channel, leading to active power generation and self-powered photodetection with record-high V_{OC} and zero bias EQE.

3 Conclusion

In summary, we have reported a unique design of $MAPbI_3/WSe_2$ device as a programmable photodiode. The $MAPbI_3$ perovskite served as not only programmable ionic dopants but also the excellent optical absorber and highly efficient sensitization layer, resulting in the record-high optoelectronic performance (V_{OC} = 1.08 V; EQE = 91.3%) among WSe_2-based lateral-structured photodiodes reported to date. Our solid ionic doping approach offers a non-invasive way to tailor the electronic properties of 2DSCs and to reversibly tune the polarities of reconfigurable photodiodes without chemical manipulation. Furthermore, a combination of atomically thin 2D materials and ionic solids enables efficient coupling between electronic transport and ionic transport, which could open a new pathway to unconventional computing, information storage systems and programmable optoelectronic devices.

4 Methods

4.1 Fabrication of $MAPbI_3/WSe_2$ transistor

The $MAPbI_3/WSe_2$ devices were fabricated by integrating PbI_2 flakes with prefabricated WSe_2 FETs followed by $MAPbI_3$ conversion process. Briefly, WSe_2 FETs were contacted with Au (30 nm) through electron-beam lithography defined patterns. The exfoliated PbI_2 flakes from its layered crystal were transferred onto the prefabricated devices through dry transfer approach we have previously reported [36]. Subsequently, the transferred PbI_2 flakes were converted to $MAPbI_3$ through vapor phase reaction with CH_3NH_3I vapor with the resulting thickness of ~ 50 nm. A few-layer h-BN flakes were transferred on top of the entire devices as encapsulation layers. The graphene-contacted devices were fabricated by transferring two parallel graphene flakes on top of an exfoliated monolayer WSe_2 flake, followed by standard electron-beam lithography and electron-beam evaporation to connect the transferred graphene with Cr/Au (20 nm/80 nm) metal electrodes.

4.2 Device poling process and characterization

To facilitate ion migration in $MAPbI_3$ perovskite, the devices were placed on the heating stage of the probe station (Lakeshore, TTP4) and heated to 400 K. After 5 min of applying poling voltages either to V_{DS} or V_{BG},

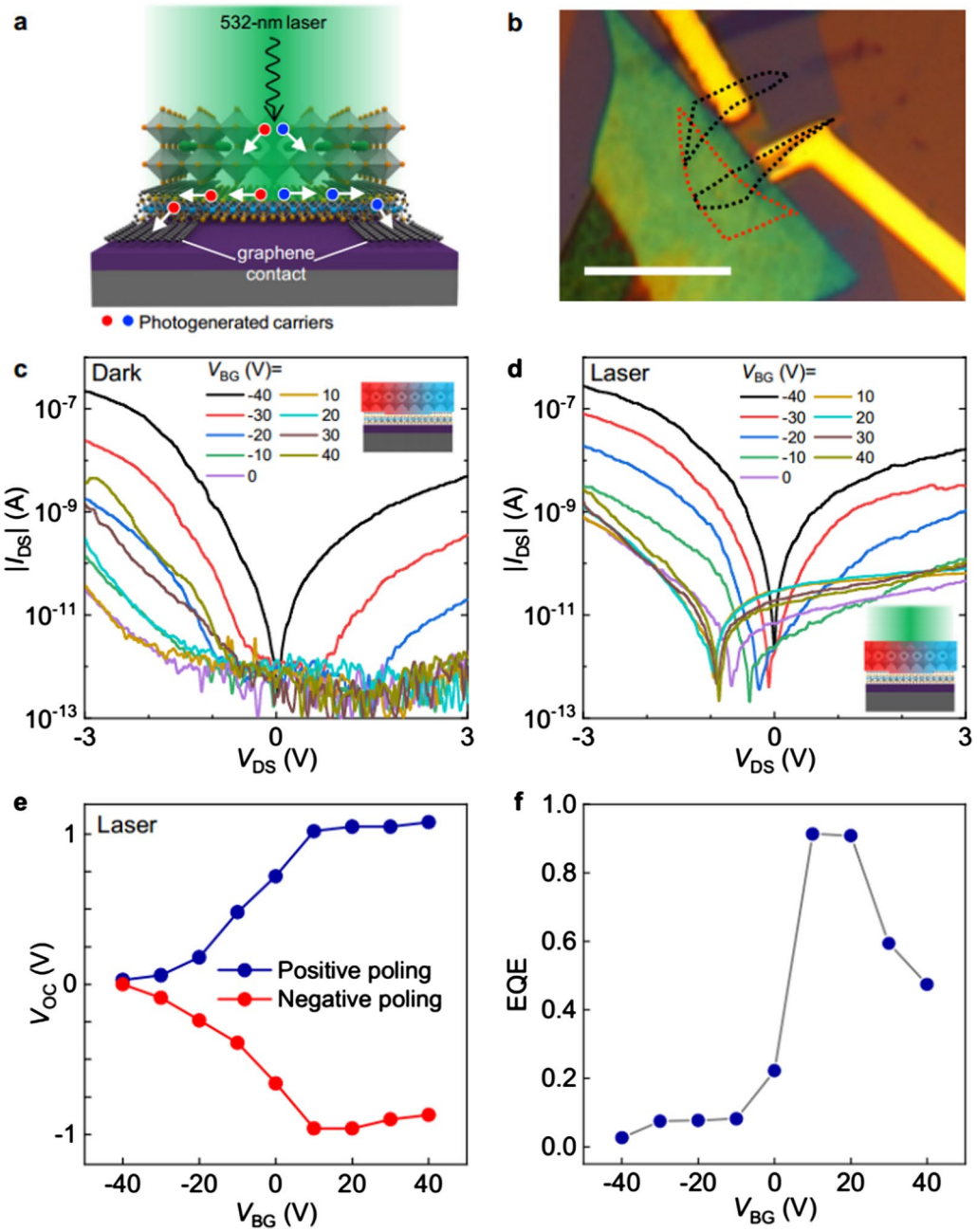

Fig. 5 Optoelectronic properties in graphene-contacted programmable $MAPbI_3/WSe_2$ photodiodes. **a** Schematic illustration of photogenerated carrier extraction in a graphene-contacted $MAPbI_3/WSe_2$ photodiode under 532-nm laser illumination. **b** Optical image of the fabricated graphene-contacted $MAPbI_3/WSe_2$ FET. The black and red dashed frames mark the position of a pair of graphene and WSe_2. The white scale bar is 10 μm. **c**, **d** Gate-tunable output characteristics (I_{DS}-V_{DS}) of the graphene-contacted device after negative lateral poling process measured under dark (**c**) and 532-nm laser illumination (**d**) conditions. The inset shows a schematic illustration of the ionic charge profile. **e** Open circuit voltages (V_{OC}) extracted from the I_{DS}-V_{DS} curves after positive (blue) and negative (red) lateral poling processes. **f** External quantum efficiency (EQE) extracted from the gate-dependent short circuit current (I_{SC}) measured from negatively poled device under 532-nm laser illumination

the devices were cooled down to 79 K. All the measurements were conducted at 79 K unless otherwise noted. The magnitude of the applied poling voltages for vertical poling by V_{BG} was 60 V. For lateral poling process by V_{DS}, 5 V was applied for about 3 μm of channel length. The poling voltages were continuously applied during the cooling process. The electrical measurements were conducted in the probe station equipped with 532-nm

wide field laser (Coherent, 532-100). The measurement data were obtained by a precision source/measure unit (Agilent, B2902A) and a computer-controlled analogue-to-digital converter.

Supplementary Information

The online version contains supplementary material available at https://doi.org/10.1186/s43593-023-00040-8.

Additional file 1: Fig. S1. Material characterization of our as-exfoliated monolayer WSe_2 for device fabrication. **a** Photoluminescence spectrum of monolayer WSe_2 under 633-nm laser showed the bright single-peak emission at 751 nm as the indirect to direct bandgap transition from few-layer to monolayer WSe_2. **b** Raman spectrum of monolayer WSe_2 under 633-nm laser showed the softening of E^1_{2g}&A_{1g} modes and the change of spectral weight in monolayer WSe_2 as compared to the few-layer WSe_2 [55]. **Fig. S2.** Schematic illustrations of van der Waals integration of $MAPbI_3$ perovskite with WSe_2 field-effect transistors (FETs). Prefabricated WSe_2 FET (**1**), PbI_2 lamination (**2**), vapor-phase conversion of $MAPbI_3$ perovskite in CVD furnace (**3**) and $MAPbI_3/WSe_2$ FET (**4**). **Fig. S3.** Single-layer WSe_2 FET before $MAPbI_3$ integration. **a** Optical image of a single-layer WSe_2 FET before integration of $MAPbI_3$ perovskite. The white scale bar is 10 μm. **b** Output characteristics (I_{DS}-V_{DS}) of the device under white light illumination and in dark. **c** Transfer characteristics (I_{DS}-V_{BG}) of the device under white light illumination and in dark. **Fig. S4**. **a** The time-domain photoresponse of the $MAPbI_3/WSe_2$ photodiode after negative lateral poling process measured under 532-nm laser illumination with 7 Hz of chopping frequency. **b** The photocurrent (I_{ph}) and response time (τ) estimated from the mean values of the current steps during on and off states. The I_{ph} and τ were extracted from part a (red dashed frame): I_{ph} ~ 83.3 pA and τ ~ 450 μs at V_{DS} = 0 V. **Fig. S5.** Negatively-poled $MAPbI_3/WSe_2$ photodiodes. **a**, **b** Output characteristics (I_{DS}-V_{DS}) of $MAPbI_3/WSe_2$ FET and $MAPbI_3$ FET measured after negative lateral poling process in dark (**a**) and under 532-nm laser illumination (**b**), showing that the diode behaviors were prominent in the device integrated with WSe_2. All the measurements were conducted at 79 K. **Fig. S6.** Gate-tunable properties of $MAPbI_3/WSe_2$ FETs. **a** Gate-dependent output curves (I_{DS}-V_{DS}) of $MAPbI_3/WSe_2$ FET with Au contact electrodes under 532-nm laser illumination. **b** The comparison of gate-dependent open circuit voltage (V_{OC}) of $MAPbI_3/WSe_2$ FET either with graphene (red) or Au (blue) contact after negative lateral poling process. **Table S1.** Summary of the photodiode parameters in different studies. Data are from this work and references [56–64].

Author contributions

XD designed and supervised the research. XD, YH, and DJK supervised the research; S-JL, and H-CC conducted experiments with assistance from YW, BZ, DL, GW, YL, JG, and HW; S-JL, and H-CC analyzed the data and prepared the figures; XD, S-JL, and H-CC wrote the manuscript with input from all coauthors. All authors reviewed and commented on the manuscript. All authors read and approved the final manuscript.

Funding

X.D. acknowledges the support from the Office of Naval Research through Grant No. N00014-22-1-2631. D.J.K. acknowledges support by the MOTIE (Ministry of Trade, Industry, and Energy) in Korea, under the Fostering Global Talents for Innovative Growth Program (P0008746) supervised by the Korea Institute for Advancement of Technology (KIAT).

Availability of data and materials

The datasets used and/or analyzed during the current study are available from the corresponding author on reasonable request.

Declarations

Competing interests

The authors declare that they have no conflict of interest.

Received: 18 November 2022 Revised: 18 January 2023 Accepted: 14 February 2023
Published online: 10 April 2023

References

1. J. Williams, L. DiCarlo, C. Marcus, Quantum Hall effect in a gate-controlled p-n junction of graphene. Science **317**, 638–641 (2007)
2. N.M. Gabor et al., Hot carrier–assisted intrinsic photoresponse in graphene. Science **334**, 648–652 (2011)
3. W.J. Yu, B.R. Kang, I.H. Lee, Y.S. Min, Y.H. Lee, Majority carrier type conversion with floating gates in carbon nanotube transistors. Adv. Mater. **21**, 4821–4824 (2009)
4. Y. Wang et al., Structural phase transition in monolayer $MoTe_2$ driven by electrostatic doping. Nature **550**, 487–491 (2017)
5. H. Zhou, Y. Du, P.D. Ye, Ionic liquid gating on atomic layer deposition passivated GaN: ultra-high electron density induced high drain current and low contact resistance. Appl. Phys. Lett. **108**, 202102 (2016)
6. M.E. Beck, M.C. Hersam, Emerging opportunities for electrostatic control in atomically thin devices. ACS Nano **14**, 6498–6518 (2020)
7. S. Jiang, L. Li, Z. Wang, K.F. Mak, J. Shan, Controlling magnetism in 2D CrI_3 by electrostatic doping. Nat. Nanotechnol. **13**, 549–553 (2018)
8. S. Liu et al., Room-temperature valley polarization in atomically thin semiconductors via chalcogenide alloying. ACS Nano **14**, 9873–9883 (2020)
9. A.Y. Joe et al., Electrically controlled emission from singlet and triplet exciton species in atomically thin light-emitting diodes. Phys. Rev. B **103**, L161411 (2021)
10. T. Roy et al., Dual-gated MoS_2/WSe_2 van der Waals tunnel diodes and transistors. ACS Nano **9**, 2071–2079 (2015)
11. J. W. Mayer, Ion implantation in semiconductors. *1973 International Electron Devices Meeting*, 3–5 (1973)
12. K. Zhang et al., Manganese doping of monolayer MoS_2: the substrate is critical. Nano Lett. **15**, 6586–6591 (2015)
13. S.-J. Lee et al., Programmable devices based on reversible solid-state doping of two-dimensional semiconductors with superionic silver iodide. Nat. Electron **3**, 630–637 (2020)
14. J.S. Ross et al., Electrically tunable excitonic light-emitting diodes based on monolayer WSe_2 p–n junctions. Nat. Nanotechnol. **9**, 268–272 (2014)
15. B.W. Baugher, H.O. Churchill, Y. Yang, P. Jarillo-Herrero, Optoelectronic devices based on electrically tunable p–n diodes in a monolayer dichalcogenide. Nat. Nanotechnol. **9**, 262–267 (2014)
16. A. Pospischil, M.M. Furchi, T. Mueller, Solar-energy conversion and light emission in an atomic monolayer pn diode. Nat. Nanotechnol. **9**, 257–261 (2014)
17. H.-P. Komsa et al., Two-dimensional transition metal dichalcogenides under electron irradiation: defect production and doping. Phys. Rev. Lett. **109**, 035503 (2012)
18. J. Shim et al., Recent progress in Van der Waals (vdW) heterojunction-based electronic and optoelectronic devices. Carbon **133**, 78–89 (2018)
19. Y. Wang, Y. Zheng, C. Han, W. Chen, Surface charge transfer doping for two-dimensional semiconductor-based electronic and optoelectronic devices. Nano Res. **14**, 1682–1697 (2021)
20. A. Rasmita, W.-B. Gao, Opto-valleytronics in the 2D van der Waals heterostructure. Nano Res. **14**, 1901–1911 (2021)
21. S.H. Yu et al., Dye-sensitized MoS_2 photodetector with enhanced spectral photoresponse. ACS Nano **8**, 8285–8291 (2014)
22. J.-W. Lee et al., Solid-phase hetero epitaxial growth of α-phase formamidinium perovskite. Nat. Commun. **11**, 5514 (2020)
23. Z. Fan et al., Layer-by-layer degradation of methylammonium lead triiodide perovskite microplates. Joule **1**, 548–562 (2017)

24. Z. Xiao et al., Giant switchable photovoltaic effect in organometal trihalide perovskite devices. Nat. Mater. **14**, 193–198 (2015)
25. G. Tumen-Ulzii et al., Hysteresis-less and stable perovskite solar cells with a self-assembled monolayer. Commun. Mater. **1**, 31 (2020)
26. S. Tan et al., Steric impediment of ion migration contributes to improved operational stability of perovskite solar cells. Adv. Mater. **32**, 1906995 (2020)
27. J. Jiang et al., Rational design of $Al2O_3$/2D perovskite heterostructure dielectric for high performance MoS_2 phototransistors. Nat. Commun. **11**, 4266 (2020)
28. J.-W. Lee, H.-S. Kim, N.-G. Park, Lewis acid–base adduct approach for high efficiency perovskite solar cells. Acc. Chem. Res. **49**, 311–319 (2016)
29. C. Eames et al., Ionic transport in hybrid lead iodide perovskite solar cells. Nat. Commun. **6**, 7497 (2015)
30. Y.-H. Kim et al., Comprehensive defect suppression in perovskite nanocrystals for high-efficiency light-emitting diodes. Nat. Photonics **15**, 148–155 (2021)
31. Y. Liu et al., Approaching the Schottky-Mott limit in van der Waals metal–semiconductor junctions. Nature **557**, 696–700 (2018)
32. H.-J. Chuang et al., High mobility WSe_2 p-and n-type field-effect transistors contacted by highly doped graphene for low-resistance contacts. Nano Lett. **14**, 3594–3601 (2014)
33. C. Sandroff, S. Kelty, D. Hwang, Clusters in solution: growth and optical properties of layered semiconductors with hexagonal and honeycombed structures. J. Chem. Phys. **85**, 5337–5340 (1986)
34. R. Cheng et al., High-frequency self-aligned graphene transistors with transferred gate stacks. Proc. Natl. Acad. Sci. **109**, 11588–11592 (2012)
35. Q. Chen et al., Planar heterojunction perovskite solar cells via vapor-assisted solution process. J. Am. Chem. Soc. **136**, 622–625 (2014)
36. H.-C. Cheng et al., van der Waals heterojunction devices based on organohalide perovskites and two-dimensional materials. Nano Lett. **16**, 367–373 (2016)
37. G. Wang et al., Wafer-scale growth of large arrays of perovskite microplate crystals for functional electronics and optoelectronics. Sci. Adv. **1**, e1500613 (2015)
38. D. He et al., High-performance black phosphorus field-effect transistors with long-term air stability. Nano Lett. **19**, 331–337 (2019)
39. Z. Qin et al., Incorporation of two-dimensional WSe_2 into $MAPbI_3$ perovskite for efficient and stable photovoltaics. J. Phys. Chem. Lett. **12**, 6883–6888 (2021)
40. Q. Fu et al., Ultrathin Ruddlesden-Popper perovskite heterojunction for sensitive photodetection. Small **15**, 1902890 (2019)
41. E.L. Unger et al., Hysteresis and transient behavior in current–voltage measurements of hybrid-perovskite absorber solar cells. Energy Environ. Sci. **7**, 3690–3698 (2014)
42. D.H. Kang et al., High-performance transition metal dichalcogenide photodetectors enhanced by self-assembled monolayer doping. Adv. Func. Mater. **25**, 4219–4227 (2015)
43. D. Li et al., Electronic and ionic transport dynamics in organolead halide perovskites. ACS Nano **10**, 6933–6941 (2016)
44. Y. Zhang, T. Oka, R. Suzuki, J. Ye, Y. Iwasa, Electrically switchable chiral light-emitting transistor. Science **344**, 725–728 (2014)
45. C.-L. Wu et al., Gate-induced metal–insulator transition in MoS_2 by solid superionic conductor LaF_3. Nano Lett. **18**, 2387–2392 (2018)
46. P. Chen et al., Approaching the intrinsic exciton physics limit in two-dimensional semiconductor diodes. Nature **599**, 404–410 (2021)
47. B. Peng et al., Achieving ultrafast hole transfer at the monolayer MoS_2 and $CH_3NH_3PbI_3$ perovskite interface by defect engineering. ACS Nano **10**, 6383–6391 (2016)
48. Y. Wang et al., Solution-processed MoS_2/organolead trihalide perovskite photodetectors. Adv. Mater. **29**, 1603995 (2017)
49. J. Lu et al., Hybrid bilayer WSe_2–$CH_3NH_3PbI_3$ organolead halide perovskite as a high-performance photodetector. Angew. Chem. **128**, 12124–12128 (2016)
50. G. Xing et al., Long-range balanced electron-and hole-transport lengths in organic-inorganic $CH_3NH_3PbI_3$. Science **342**, 344–347 (2013)
51. W.J. Yu et al., Vertically stacked multi-heterostructures of layered materials for logic transistors and complementary inverters. Nat. Mater. **12**, 246–252 (2013)
52. Y. Liu et al., Toward barrier free contact to molybdenum disulfide using graphene electrodes. Nano Lett. **15**, 3030–3034 (2015)
53. W.J. Yu et al., Highly efficient gate-tunable photocurrent generation in vertical heterostructures of layered materials. Nat. Nanotechnol. **8**, 952–958 (2013)
54. X. Cui et al., Multi-terminal transport measurements of MoS_2 using a van der Waals heterostructure device platform. Nat. Nanotechnol. **10**, 534–540 (2015)
55. E. Del Corro et al., Excited excitonic states in 1L, 2L, 3L, and bulk WSe_2 observed by resonant Raman spectroscopy. ACS Nano **8**, 9629–9635 (2014)
56. D.J. Groenendijk et al., Photovoltaic and photothermoelectric effect in a double-gated WSe_2 device. Nano Lett. **14**, 5846–5852 (2014)
57. M. Massicotte et al., Dissociation of two-dimensional excitons in monolayer WSe_2. Nat. Commun. **9**, 1633 (2018)
58. M.S. Choi et al., Lateral MoS_2 p–n junction formed by chemical doping for use in high-performance optoelectronics. ACS Nano **8**, 9332–9340 (2014)
59. H. Wang et al., Approaching the external quantum efficiency limit in 2D photovoltaic devices. Adv. Mater. **34**, 2206122 (2022)
60. S. Wi et al., High blue-near ultraviolet photodiode response of vertically stacked graphene-MoS_2-metal heterostructures. Appl. Phys. Lett. **104**, 232103 (2014)
61. F. Wu et al., High efficiency and fast van der Waals hetero-photodiodes with a unilateral depletion region. Nat. Commun. **10**, 4663 (2019)
62. C. Fang et al., High-performance photodetectors based on lead-free 2D Ruddlesden-Popper perovskite/MoS_2 heterostructures. ACS Appl. Mater. Interfaces. **11**, 8419–8427 (2019)
63. Z.-X. Zhang et al., Ultrafast, self-driven, and air-stable photodetectors based on multilayer $PtSe_2$/perovskite heterojunctions. J. Phys. Chem. Lett. **9**, 1185–1194 (2018)
64. Y. Chen et al., High-performance photovoltaic detector based on $MoTe_2$/MoS_2 van der Waals heterostructure. Small **14**, 1703293 (2018)